Tuning the electronic and magnetic properties of antimonene nanosheets via point defects and external fields: first-principles calculations

This article can be cited before page numbers have been issued, to do this please use: A. Bafekry, M. Ghergherehchi and S. Farjami Shayesteh, *Phys. Chem. Chem. Phys.*, 2019, DOI: 10.1039/C9CP01378D.

ROYAL SOCIETY
OF CHEMISTRY

rsc.li/pccp

ARTICLE TYPE

Tuning the electronic and magnetic properties of antimonene nanosheet via point defects and external fields: A first-principles calculations

Asadollah Bafekry,*[a] [b] Mitra Ghergherehchi* [c] Saber Farjami Shayesteh [a]

Defects are inevitably present in materials, and their existence in a material strongly affects its fundamental physical properties. We have systematically investigated the effects of surface adsorption, substitutional impurity, defect engineering, electric field and strain engineering on the structural, electronic and magnetic properties of antimonene nanosheets, using spin-polarized density functional calculations based on first-principles. The adsorption or substitution of atoms can locally modify the atomic and electronic structures as well as induce a variety of electronic behaviors including metal, half-metal, ferromagnetic metal, dilute magnetic semiconductor and spin-glass semiconductor. Our calculations showed that the presence of typical defects (vacancies and stone-wales defect) in antimonene affects the geometrical symmetry as well as the band gap in the electronic band structure and induces magnetism to antimonene. Moreover, by applying external electric field and strain (uniaxial and biaxial), the electronic structure of antimonene can be easily modified. The calculation results presented in this paper provide fundamental insight into the tunable nature of the electronic properties of antimonene, supporting its promis for use in future applications.

1 Introduction

Graphene[1] as a two-dimensional material (2DM) with crystal lattice of carbon atoms, has recently attracted a substantial interest. 2DM forms a large material family involving various kinds of layered crystal structures with chemical elements, and these materials show unique properties quite distinct from their 3D bulk structures. Hexagonal boron-nitride and transition metal dichalcogenides have been exploited from layered bulk materials.[2–7] Typical 2DM, include graphene[8,9], monolayers from group IV elements involving silicene, germanene and stanene[10–14], and group-VA layered materials such as phosphorene.[15,16] Despite the fact that 2DM hold great potential for a wide range of applications, it will be necessary to modulate their intrinsic properties before using them in real applications. Many approaches have been developed to tune the electronic and magnetic properties of 2DM. Surface functionalization with adatoms and typical defects[17–28] offers a robust approach to handle the electronic properties of 2DM. Recently, arsenene and antimonene which

have a 2D crystal honeycomb lattice similar to graphene, have emerged as a family of 2DM from group-VA layered materials which have potential applications in difference devices.[29–33] In particular, antimonene has been successfully synthesized by various strategies.[31,32,34]? Moreover, difference of theoretical calculations have been performed on first-principles studies of arsenene and antimonene.[35–42]

Several approaches have been developed to modify the electronic properties of arsenene and antimonene. These include chemical modification of the physical and chemical properties of arsenene and antimonene[43–47], which might have important applications in optoelectronic and other low dimensional applications. Other methods involving surface functionalizing with atoms and molecules[48–51], substitution doping of atoms[52–55], defects engineering[56–58], applying electric field and strain[59–63], and edge states[64,65] have been developed and these methods are used to tune the properties of heterostructures.[66–69]

In this paper, we used first-principles calculations based on density functional theory (DFT), to undertake an extensive analysis of the effects of the adsorption and substitution of atoms, including nonmetallic adatoms such as H, B, C, N, O, F, P, and Al; alkali metals (AM) (Li, Na, and K); alkaline earth metals (AEM) (Be, Mg, and Ca); and 3d transition metals (TM) (Sc, Ti, V, Cr, Mn, Fe, Co, Ni, Cu, Zn) atoms, on the structural, electronic, and magnetic properties of antimonene. Following adatom adsorp-

[a] Department of physics, University of Guilan, 41335-1914, Rasht, Iran; E-mail: Bafekry.asad@gmail.com

[b] Department of Physics, University of Antwerp, Groenenborgerlaan 171, B-2020 Antwerp, Belgium.

[c] College of Electronic and Electrical Engineering, Sungkyun kwan University, Suwon, Korea; E-mail: mitragh@skku.edu

tion, the structural geometry of antimonene can either remain the same of undergo a local lattice deformation. The adatom adsorption or substitution of atoms may induce novel electronic and magnetic behavior, including metallic, half-metallic, and dilute-magnetic semiconductor, depending on the kinds of atoms. The results of our calculations show, that the presence of topological defects including vacancies and stone-wales, changes the geometrical symmetry and modifies the electronic properties of antimonene. Defect engineering leads to the discovery of potentially exotic properties, which makes the antimonene fertile for future investigations and emerging technological applications with precisely tailored properties. In addition, we investigated the effects of charging and strain with fully relativistic calculations. The results indicate that the electronic structure of antimonene is sensitively dependent on the type and strength of strain. An indirect-direct band gap transition can occur by applying the uniaxial or biaxial strain in the tensile state, while a semiconductor-metal transition can occur in the compression state. Generally, the presence of point defects including vacancy, impurity, and interstitial atoms, in 2DM is an efficient approach and of fundamental importance because facilitating the tailoring of the resulting electronic properties can be used to effectively modify the intrinsic characteristics for subsequent use for a wide range of applications.

2 Computational Methodology

In this work, we carried out first-principle calculations, within the Perdew-Burke-Ernzerhof variant of the generalized gradient approximation (PBE-GGA)[70] method in order to deal with the exchange-correlation functionals with OpenMX code.[71,72] We used norm-conserving pseudopotentials,[73] where the wave functions are expanded in a linear combination of multiple pseudo-atomic orbitals (LCPAOs) generated using a confinement scheme.[72] After the convergence tests in OpenMX, we chose the energy cutoff of 300 Ry, such that the total-energies converge below 1.0 meV/atom. All of the structures considered were fully relaxed until the force convergence acting on each atom was less than 1 meV/Å. The charge transfer was calculated using Mulliken charge analysis.[74] We calculated electronic structure using different codes including Quantum Expresso[75], SIESTA,[76] and ABINIT[77]. The **k**-points for sampling over the Brillouin zone (BZ) integration were generated using the Monkhorst-Pack scheme.[78] For a primitive cell of hexagonal antimonene, a **k**-mesh grid of $15 \times 15 \times 1$ was used and scaled according to the size of the supercells for OpenMX and SIESTA codes, while the Brillouin zone (BZ) was sampled by a **k**-mesh grid of $21 \times 21 \times 1$ for Quantum Expresso and ABINIT codes. The antimonene are modeled as a supercell with a sufficiently large vacuum space of 20 Å along the z-direction in order to avoid interactions between adjacent layers in all of the codes. Simulated scanning tunneling microscopy (STM) images were obtained using the Tersoff-Hamann theory[79], as supplied with the OpenMX code, which obtainns images with a bias of +2.0 V that were graphed using WSxM software.[80]

3 Pristine Antimonene

The honeycomb atomic structure of antimonene, is buckled with the space group of P_{3m1}, as shown in Fig.1 (a). The lattice constant of antimonene is determined to be 4.12 Å, while Sb-Sb bond length, the buckling (height between two sublattices) and bond angle are found to be 2.95, 1.75 Å, and 88°, respectively. These values are consistent with previous calculation results.[41,49,55] The difference and total charge densities are also shown in Fig. 1(a). We can observe a high charge density around Sb atoms, which indicates that the bonding between Sb-Sb is a covalent bond character. From the STM image shown in Fig. 1(b), we can see that the Sb atom in one sublattice is brighter than that in another sublattice. The stability of antimonene is investigated by calculating the phonon dispersion by Quantum Expresso code, and the obtained dispersion curve is shown in Fig. 1(c). No imaginary vibrating mode is seen, demonstrating their stability as free-standing antimonene, which is consistent with the results of a previous studies.[24,40]

The electronic structure with corresponding density of states (DOS) of antimonene, is shown in Fig. S1 (see supplementary information (SI)). Our results show that antimonene is an indirect semiconductor with a 1.02 eV band gap, while the valence band maximum (VBM) and conduction band minimum (CBM) are located at Γ and **M** points in the Brillouin zone, respectively. The band gap decreases to 0.76 eV when the spin-orbit coupling (SOC) is added to the calculation. Our calculated band gap is consistent with previously reported results.[49,81] Based on observed the orbital resolved band structure, it is clear that the electronic state is mainly made up of s and p-orbitals (see Fig. 1(d)). Three branches of bands are evident, and they are indicated by different colors. The lower branch mainly consists of s-orbitals, while the other two branches mainly consist of p-orbitals. We can see from both the band structure and PDOS that the ranges of all of these three energy bands shrink, indicating the weakening of interactions between orbitals as the covalent bonds become longer. Moreover, we calculated the DOS and band structure of antimonene with QUANTUM ESPRESSO in plane-wave, ABINIT with plane-augmented-wave and SIESTA with numerical atomic orbitals (NAO) basis set (see Fig. 1(e)). One can see, that antimonene is an indirect semiconductor by using QUANTUM ESPRESSO, ABINIT, and SIESTA calculations, and this observation is very similar to that of OpenMX. The intensity map of the band structure is calculated by OpenMX and QUANTUM ESPRESSO and is shown in Fig. 1(f).

4 Adsorption of adatom

In order to investigate the effects of adatom adsorption on antimonene, all of the considered adatoms are initially placed at a height of ~ 2Å from the surface of antimonene on four possible favorable adsorption sites, shown in Fig. 2(a). The possible adsorption sites are as follows: (1) the top site (T-site), where the adatom is on top of an Sb atom, (2) the bridge site (B-site), where the adatom is above the center of the Sb-Sb bond, (3) the hollow site (H-site), where the adatom is located above the center of hexagonal Sb atoms, (4) the valley site (V-site), where the adatom is placed on top of the low-buckled Sb atom. Hereafter, the adatom adsorbed on antimonene will label as Ad/ant. After performing the full structure optimization, the energetically favorable adsorption site for the considered adatoms is de-
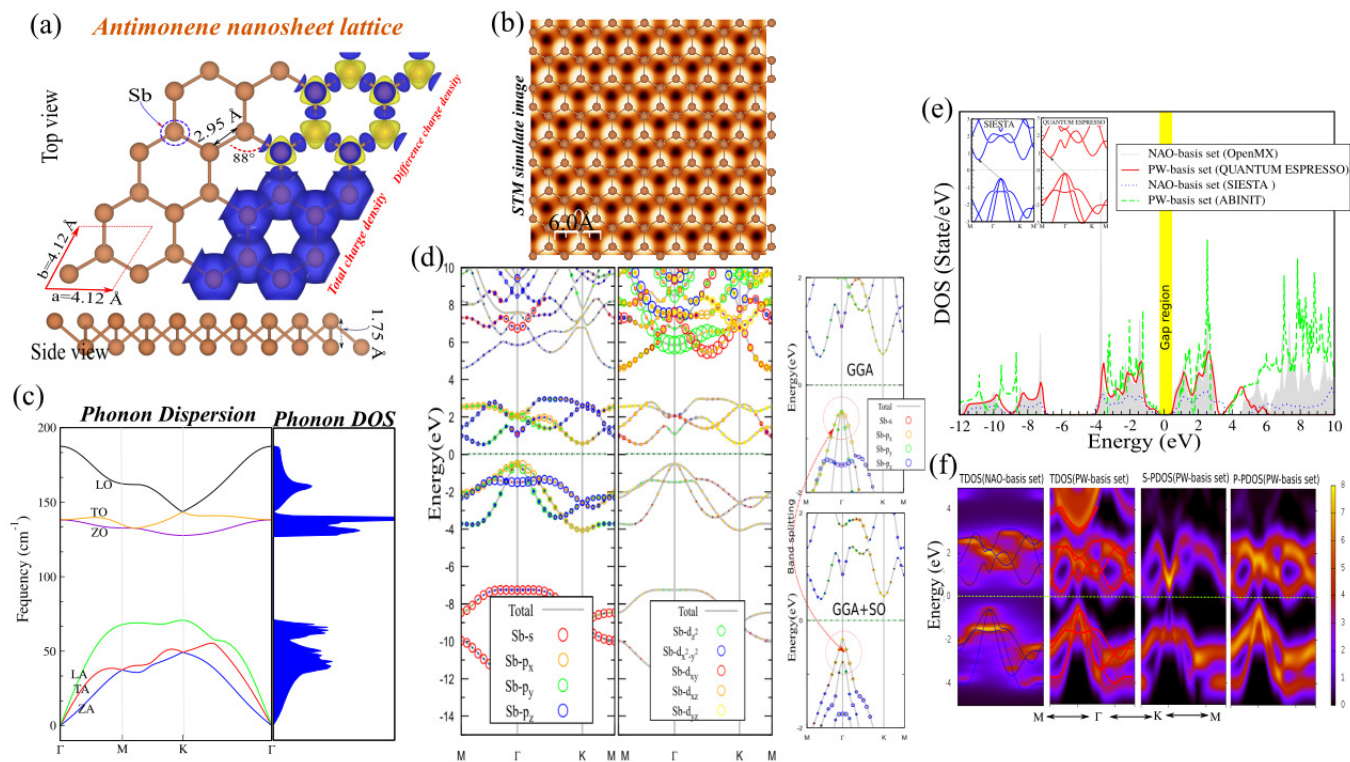
Fig. 1 (a) Optimized structure of antimonene, with its hexagonal primitive unit cell, indicated by a red parallelogram. The brown dot is an Sb atom. The total and different charge density are also shown in the same panel. (b) Simulated STM image. Inset structure represents antimonene repeating unit cell. (c) Phonon dispersions of antimonene. (d) Orbital resolved band structure without/with SOC effect. (e) DOS and band structures of antimonene as calculated with OpenMX, QUANTUM ESPRESSO, SIESTA and ABINIT codes. (f) Intensity map of electronic band structure calculated by OpenMX and QUANTUM ESPRESSO. The zero of energy is set to the Fermi level (E_F).

termined to have the lowest ground state energy configuration among the four adsorption sites. The adsorption energy is defined $E_a = E_{antimonene} + E_{Ad} - E_{Ad/ant}$, where $E_{Ad/ant}$ is the total energy of the Ad/ant system, $E_{antimonene}$ is the total energy of the pristine antimonene, and E_{Ad} is the total energy of an isolated adatom in vacuum. Variations in the structural and electronic parameters including adsorption energy, bond length, height, band gap, and magnetic moment for adatoms adsorption on antimonene, are shown in Figs. 2(b-f)

Th optimized structures of Ad/ant (Ad= H, O, S, F, Cl, B, C, Si, N, and P) at the stable site are shown in Fig. 3. For H, F, Cl, and P adatoms, the T-site is a stable site, while the B, C, Si and N adatoms are adsorbed at the V-site. The O and S adatoms are located on the B-site (see Fig. 3). Upon the adsorption of these adatoms, a local distortion in the structure of antimonene can occur. In these stable sites, adatoms form covalent bonds with the nearest Sb atoms, which leads to the Sb atom moving of the antimonene plane. The adsorption energies of H, F, Cl, and P adatoms are in the range of 1.6-3.3 eV. The d_{A-Sb} is $\sim$ 1.80-2.78 Å while d_{Sb-Sb} is elongated $\sim$ 2.98 Å, as compared with pristine antimonene. Following relaxation, the calculated heights of the adatoms are about 2.92-3.72 Å (see Figs. 2(a-c)). These results are good consistent with those previously reported in the literature.[47,49] The optimized structures of Ad/ant (Ad= Al, Li, Na, K, Be, Mg, and Ca) are shown in Fig. 3. The Li, Na, K, Mg, Ca, and Al are adsorbed at the stable V-site, while Be, is adsorbed

at the stable B-site.

By contrast, in the H, O, S, F, C, Si, N, and P adatoms, which cause strong distortions in the antimonene structure, the adsorption of Li, Na, K, Be, Mg, Ca, and Al adatoms to antimonene, due to the weaker interaction between adatoms and antimonene, does not yield any significant distortion. Accordingly, the calculated adsorption energies of these adatoms adsorbed to antimonene at stable sites, range from 1.2-2.5 eV and have a larger $d_{A-Sb} = 2.32-3.53$ Å. The height of adatoms, calculated as the difference between the average coordinates of neighboring Sb atoms and the adatom, is 1.02-4.08 Å. In addition the adatoms do not have an effect on the shifting of neighboring Sb atoms, and the buckling in the plane is negligible (see Figs. 2(b-d)). Our results are consistent with those of previous reports.[49,51] It is also found that height increases from Li to K adatoms due to the increasing atomic radius. Typically, the impurity adatom with a relatively large effective decay radius, will lead to a small adsorption energy, because a larger effective decay radius indicates a more intense localization of impurity states. We can see from the adsorption energy and structural parameter, in the situation that d_{A-Sb} is large (short), the E_a tends to decrease (increase) and the adatom shows physical (chemical) adsorption. In order to further understand the bond character, the differential charge density is shown in Fig. 3 in the same panel. Not that there is a charge accumulation in the region between adatoms and neighboring Sb atoms, which is the result of the strong covalent bond character
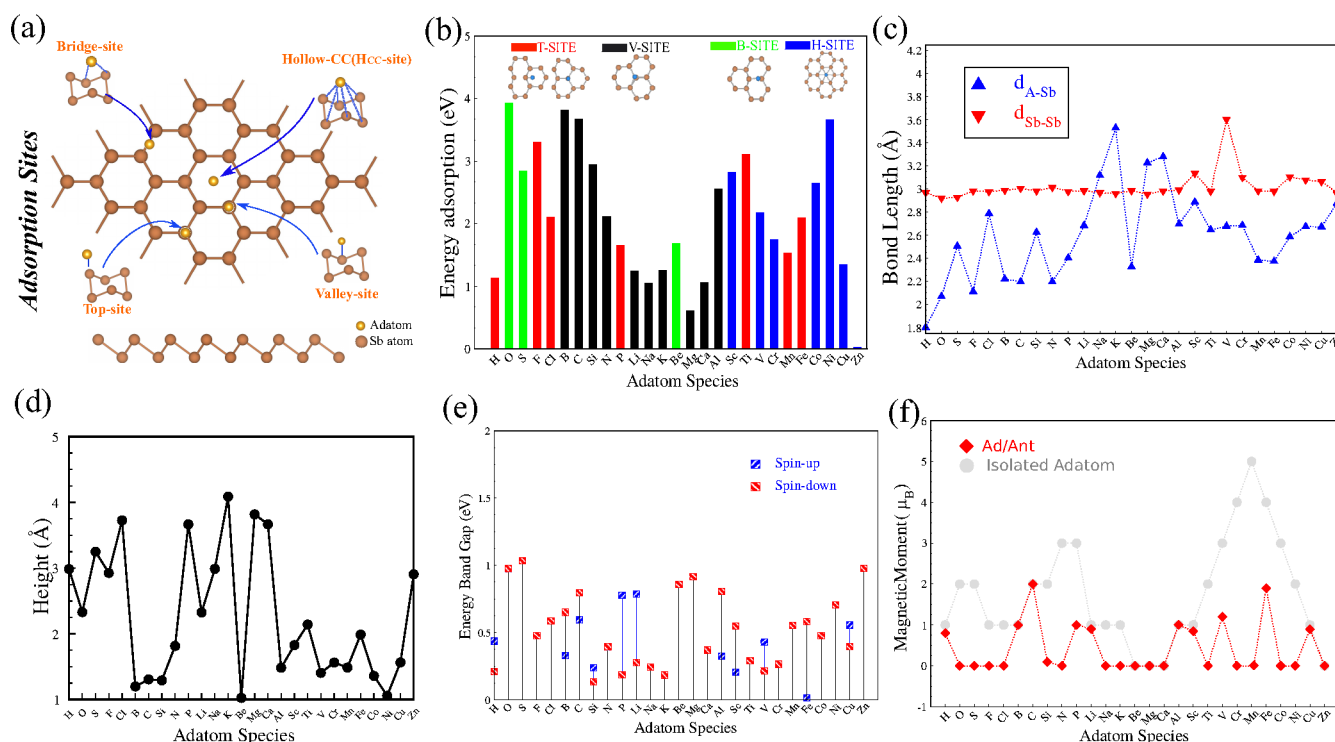
Fig. 2 (a) Schematic view of possible adatom adsorption sites on antimonene. Variations of structural parameters including (b) adsorption energy, (c) bond length between adatom and its nearest atom d_{A-Sb} with the bond length between Sb-Sb atoms d_{Sb-Sb}, (d) height of adatom from the antimonene plane. Variations of electronic parameters including (e) energy band gap of HOMO-LUMO and (f) magnetic moment for adatoms adsorption on antimonene

in the formed d_{A-Sb}. From this, we can see that strong electron depletion happens on the adatom while extremely local electron gain occurs on the Sb atoms of hexagon, which demonstrates the weakly covalent character of d_{A-Sb}. In addition, the transfer of charge between adatoms and antimonene is 0.14 eV, and 0.21 eV for Li and K, respectively.

Now, we explore the electronic and magnetic properties of Ad/ant. The band structure and DOS of Ad/ant (Ad= H, O, S, F, Cl, B, C, Si, N, P, Al, Li, Na, K, Be, Mg, and Ca adatoms), is shown in Fig. 4. We can see that electronic structure of the pristine antimonene is modified by the adsorption of these adatoms. The energy bands around E_F, mainly occur from the adatoms orbital states and shown as localized impurity states. For H/ant, the system remains as a semiconductor with a direct band gap of 0.24 eV for the spin-up (↑) channel, whereas the spin-down (↓) channel has the metallic state. Thus, the density of ↑ and ↓ spin channels show spin polarization and becomes a half-metal. The O and S/ant exhibit a semiconductor with 0.95 and 1.02 eV band gaps, respectively, while in F, Cl and N/ant, the semiconducting band gap of antimonene is eliminated and metallic behavior in induced due to the impurity states around the E_F. These results are good consistent with those previously reported in the literature.[47,49] Our results show that B, C, and P/ant exhibit a dilute-magnetic semiconductor with 1, 2 and 1 μ_B magnetic moments, respectively. This interesting character may have potential for the design of new spintronic devices using antimonene-based material. The Si/ant becomes a ferromagnetic-metal and has a

0.3 μ_B magnetic moment (see Fig. 4 and Figs. 2(e,f)). We can see that the adsorption of Be, Mg, and Ca adatoms preserves the semiconducting behavior of antimonene, while Li, Na, K, and Al modify the electronic state of antimonene. Meanwhile the Li energy bands split into ↑ and ↓ spin channels and exhibit a dilute-magnetic semiconductor with 0.9 μ_B magnetic moment in ground state.

For Na and K/ant, impurity states appear around E_F and exhibit a metallic character. Following the adsorption of the Be, Mg, and Ca, we can see a semiconducting behavior with a ~ 0.85 eV band gap in electronic band (see Fig. 4 and Figs. 2(e,f)). The Al/ant exhibits a spin-glass semiconductor, specially with a gapless ↑ spin channel, while the ↓ spin channel is semiconductor, and the degeneracies of the ↑ and ↓ spin states are broken and induce 1 μ_B to the structure. These results are consistent with previous calculations.[49,51] Compared with pristine antimonene, the shape of the DOS of Ad/ant is substantially changed due to the strong disturbance of the s and $p_{x,y}$-orbitals caused by the adatom.

Based on the DOS and PDOS shown in Fig. 5, we found that the VBM of Ad/ant (Ad= H, O, S, B, C, Si, N, and P) can be attributed to the hybridization of s and $p_{x,y}$ of adatoms and $p_{x,y}$-orbitals of the nearest Sb atoms. For F and Cl/ant, it is clear that the interaction between adatom and antimonene may be determined by adatom $p_{x,y}$-orbital states rather than s and $p_{x,y}$-states, and metallic behavior comes from $p_{x,y}$-orbitals. In O/ant, the VBM main contribution comes from O-$p_{x,y}$ and Sb-$p_{x,y}$ orbitals hybridization and O-p_z orbital does not mix with surrounding Sb

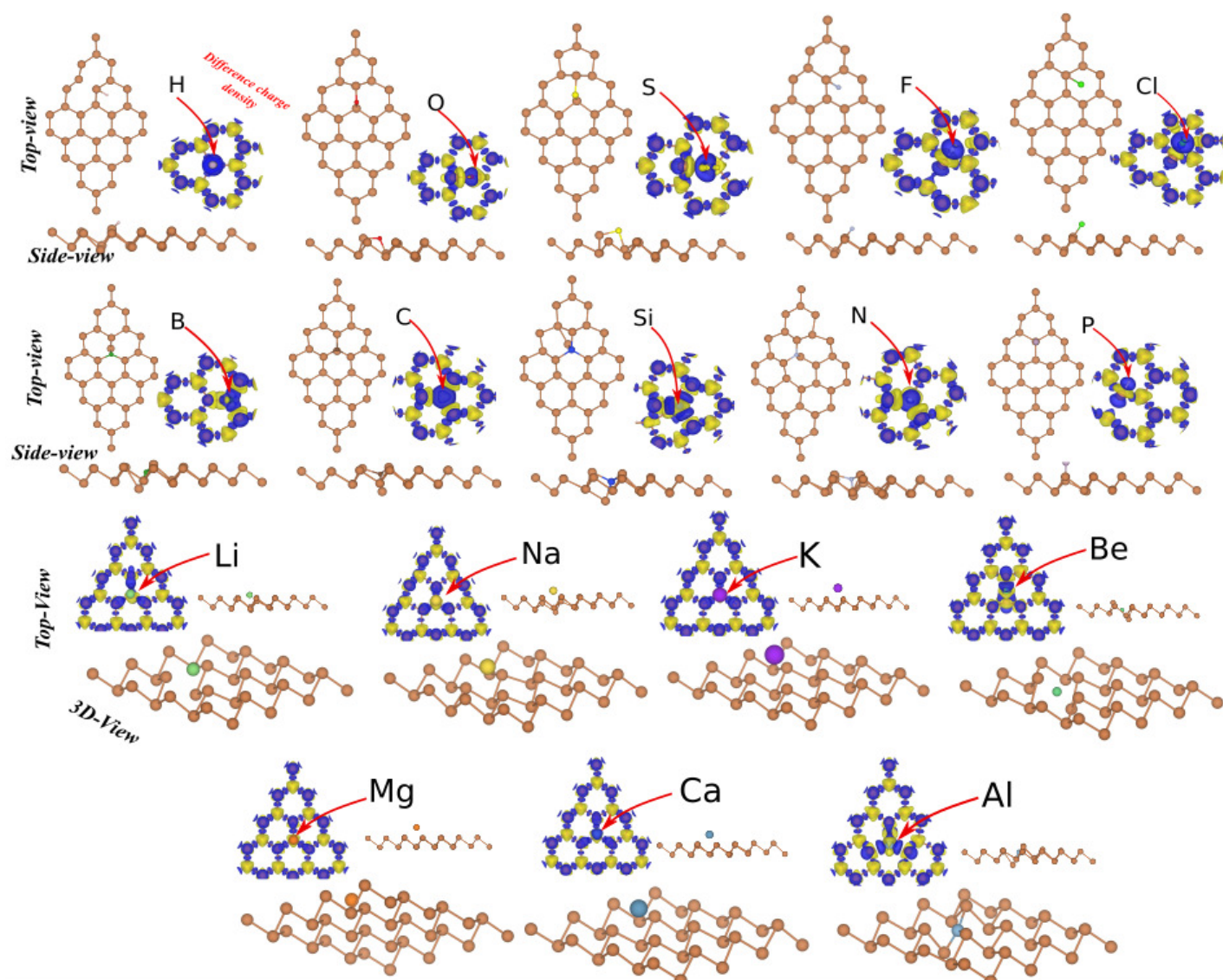Physical Chemistry Chemical Physics Accepted Manuscript

Fig. 3 (a) Optimized structures for adsorption of H, O, S, F, Cl, B, C, Si, N, P, Al, Li, Na, K, Be, Mg and Ca adatoms on antimonene at stable sites. The difference charge density indicated as same panel. The blue and yellow regions represent the charge accumulation and depletion, respectively.

states. While the CBM is formed by the hybridization of p_z orbital of O adatom and Sb atom of antimonene. For the B/ant, the VBM main contribution comes from B-p_z with Sb-$p_{x,y}$ orbitals hybridization, whereas B-$p_{x,y}$ and Sb-p_z orbitals do not mix. The CBM of both B and Sb is formed by the hybridization of $p_{x,y}$-orbital states. Based on PDOS shown in Fig. 6(b), the VBM and CBM of Li, Na, K, and Mg/ant are attributed to the hybridization of Sb-$p_{x,y}$ with the adatom-s orbital states around E_F, whereas adatom-$p_{x,y,z}$ does not mix with Sb orbital states. It can be seen that that due to the charge transfer, E_F is shifted for these systems. The present results show that the metallic characteristic of Be, Ca, and Al/ant, are mainly originated from adatom-s and Sb-$p_{x,y}$ orbital states of antimonene.

The optimized structures of the 3d transition metal (TMs) atoms adsorbed antimonene (TMs/ant) at stable sites are shown in Fig. S2. The Sc, V, Cr, Co, Ni, and Zn adatoms bind to antimonene on stable H-site, while the Ti, Mn and Fe are located

above one of the Sb atoms in the antimonene. In contrast to the AM and AEM adatoms, the adsorption of TMs adatoms to antimonene, can result in relatively stronger interaction between TMs and antimonene, as well as the adsorption energy range of 1.3-3.6 eV. The d_{A-Sb}, bond distance is in the range of 2.37-2.88 Å and the height of adatoms are relatively small, at about 1.05-2.90 Å (see Figs. 2(b-d)). These results are with those that have been previously reported in the literature.[47,49] The electronic structures with corresponding DOS and PDOS of TM/ant at stable sites, are shown in Figs. 6(a,b). Due to the fact that all of the 3d-TM atoms have partially occupied 3d-orbital shells, we found a variety of electronic properties. The Ti, Cr, and Zn/ant exhibit a semiconductor with about 0.5-1 eV band gaps, while the Sc, V, and Cu/ant, exhibit a dilute-magnetic semiconductor with 0.8, 1.2, and 0.9 μ_B magnetic moments, respectively. The DOS and PDOS of TM/ant at stable sites, are shown in Fig. 6(b). We can see that the states around E_F mainly originate from the
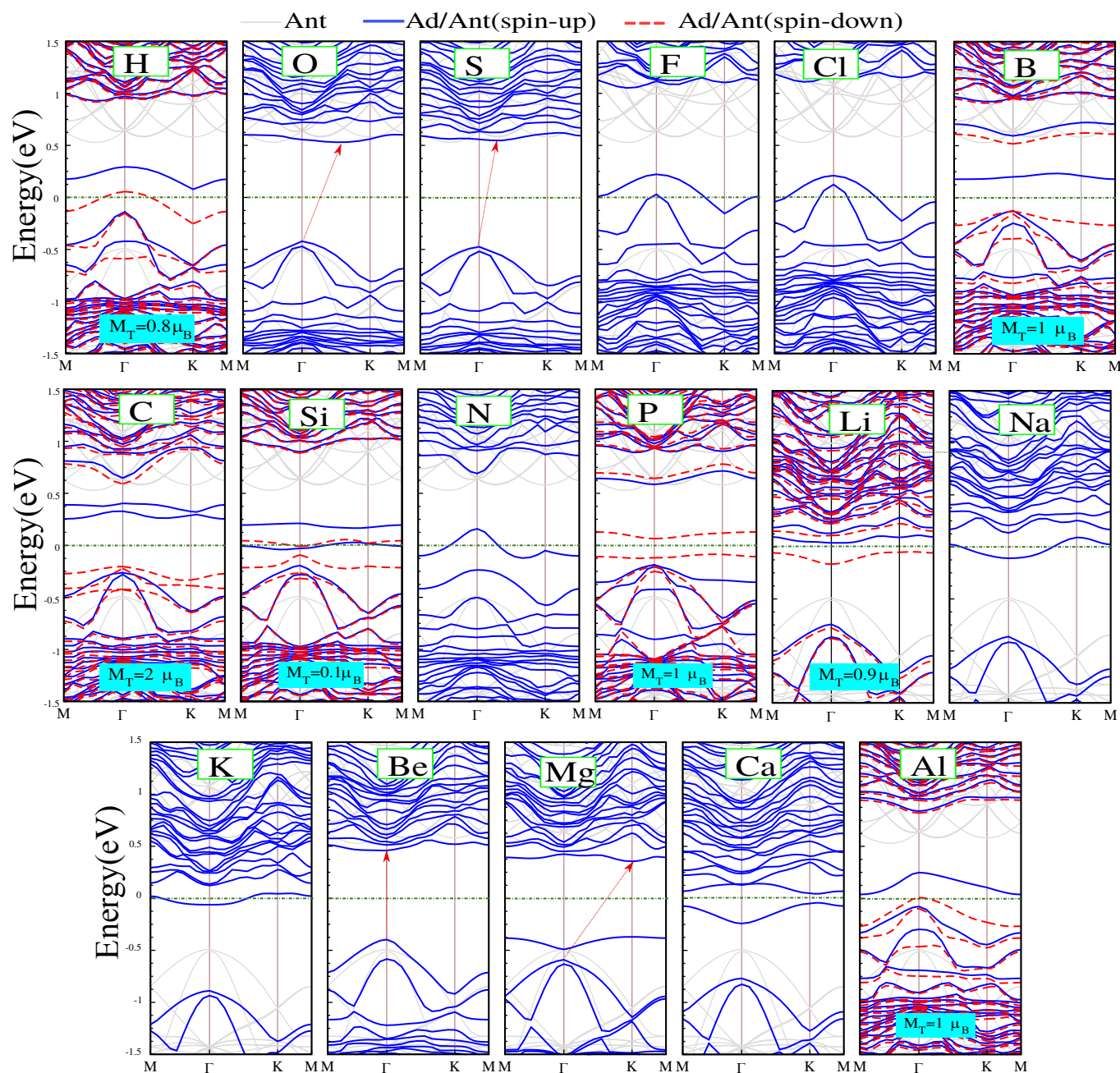
Fig. 4 Electronic structure for the adsorption of H, O, S, F, Cl, B, C, Si, N, P, Al, Li, Na, K, Be, Mg and Ca adatoms on antimonene at stable sites. The zero of energy is set to the E_F.

hybridization of TM-$d_{xy}/d_{x^2y^2}$ and the Sb-$p_{x,y}$ orbital states. For Ti/ant, main contribution of the VBM comes from Ti-z^2 with Sb-$p_{x,y}$ orbitals hybridization, while the CBM is originated from the Ti-z^2 orbital state. our result shows that, with the Mn and Co adsorption, the system becomes a metal (see Figs. 6 (a,b)). The metallic state originates from Co-$d_{xy}/d_{x^2y^2}$ orbital states at the E_F, while the metallic energy bands of the Mn/ant originates from the Mn-$d_{xy,xz}/d_{x^2y^2}$ orbital states. For Fe/ant, the configuration remains metal (direct semiconductor with 0.25 eV band gap) in the electron ↑ (↓) spin channel, which results in it becoming a half-metal. This suggests that the charge carriers around E_F are mobile, which is not only useful for conductive behavior but also

for magnetic coupling.

In order to analyze the magnetism, the difference spin densities of Ad/ant (Ad= H, B, C, Si, P, Li, Al, Sc, V, Fe, and Cu), are shown in Fig. 7. The difference spin density is calculated from the spin density difference between the ↑ and ↓ spin channels. One can conclude that the magnetism mainly originates from the these adatoms and its Sb neighbors on the antimonene. The variation of magnetic moment for Ad/ant systems, is shown in Fig. 2(f).

5 Topological defects

In this section, we consider vacancies and stone-wales defects in antimonene. We removed one Sb atom from the structure to pro-
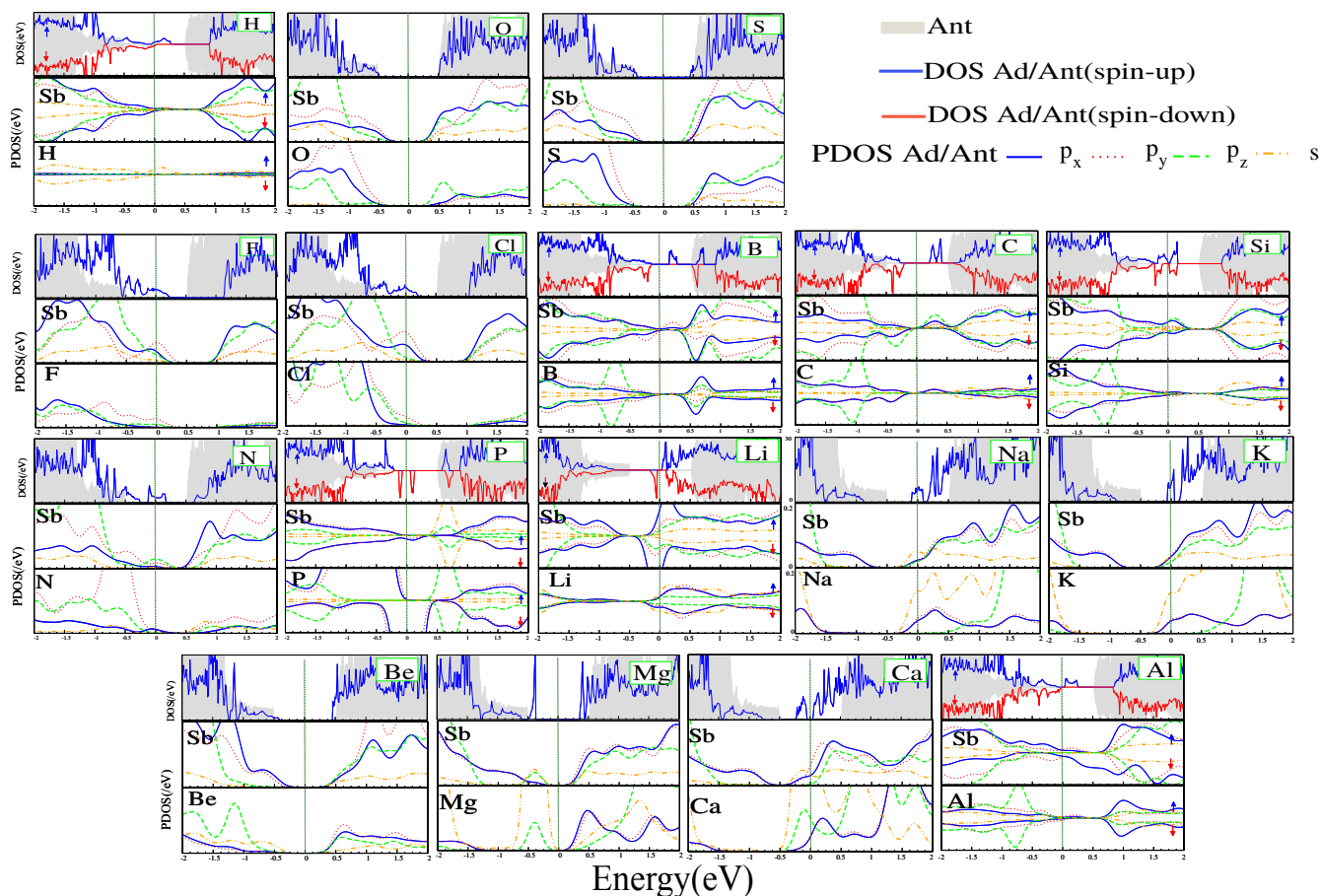
Fig. 5 DOS and PDOS for adsorption of H, O, S, F, Cl, B, C, Si, N, P, Al, Li, Na, K, Be, Mg and Ca adatoms on antimonene at stable sites. The zero of energy is set to the E_F.

duce a single vacancy in antimonene (SV-ant). In order to create a divacancy in the antimonene, we considered two different defect types. For these defects, we removed two Sb atoms, which are at the same sublattice labeled as DV1-ant and from different sublattice labeled as DV2-ant. We rotate a single Sb+Sb bond in the antimonene by 90°, resulting in a structure with a pair of seven-membered and five-membered rings. The defective structures are fully relaxed, then accurate total energies and band structures are calculated.

The optimized structures with corresponding bond lengths and bond angles for topological defects including vacancies and Stone–Wales on antimonene are shown in Figs. 8(a-d). The Sb atoms around the vacancy in antimonene undergo a Jahn-Teller distortion,[82] then Sb atoms which are near the vacancy site move towards each other so as Sb-Sb bonds. Following optimization, for reconstructed SV, two Sb atoms around the vacancy are bonded together to build a pentagon and nonagon structure (the 5-9 configuration), so the Sb-Sb bond length changed to 2.954 Å and the pentagon ring changed to 3.155 Å. By missing a pair of adjacent Sb atoms, DV-ant is formed without dangling bonds. Similar to the Sb atoms around the SV-ant, those for DV-ant undergo a Jahn-Teller distortion, and Sb atoms near the vacancy site move towards each other to form an Sb-Sb bond. In DV1-ant, we have observed no deviation from the planar configura-

tion upon structural relaxation, and it shows a non-reconstructed structures, whereas DV2-ant shows a reconstructed structure and two Sb atoms bonded together to build two pentagon structures and one heptagon structure (the 5-8-5 configuration). The distance between bonds around of the DV1-ant and DV2-ant defects are shown in Figs. 8(b,c). For the relaxed DV2-ant, we can see that the bond lengths of Sb-Sb atoms is changed. As shown in from Fig. 8(d), after the formation of the SW-ant defect, four neighboring hexagons of antimonene are transformed into one pentagon and two heptagon (the 55-77 configuration) and the antimonene maintains its planar 2D structure. Through the 90° rotation of a dimer, the Sb-Sb bond becomes stronger than it is in antimonene and its length decreases from 2.95 to 2.90 Å. The difference charge densities of defected antimonene are presented in the same panels in Figs. 8(a-d). We can see, an obvious charge accumulation in the region around the defects on antimonene, which is the result of a strong covalent bond character in the formed Sb bond. These results are consistent with those presented in previous studies.[34,52,57]

The electronic structure, DOS and PDOS of defected antimonene are shown in Figs. 8(e-h). The SV-ant exhibits a ferromagnetic-metal and has a 0.32 μ_B magnetic moment due to the dangling bonds around the single vacancy. From the DOS and PDOS shown in the same panel, we found that the state
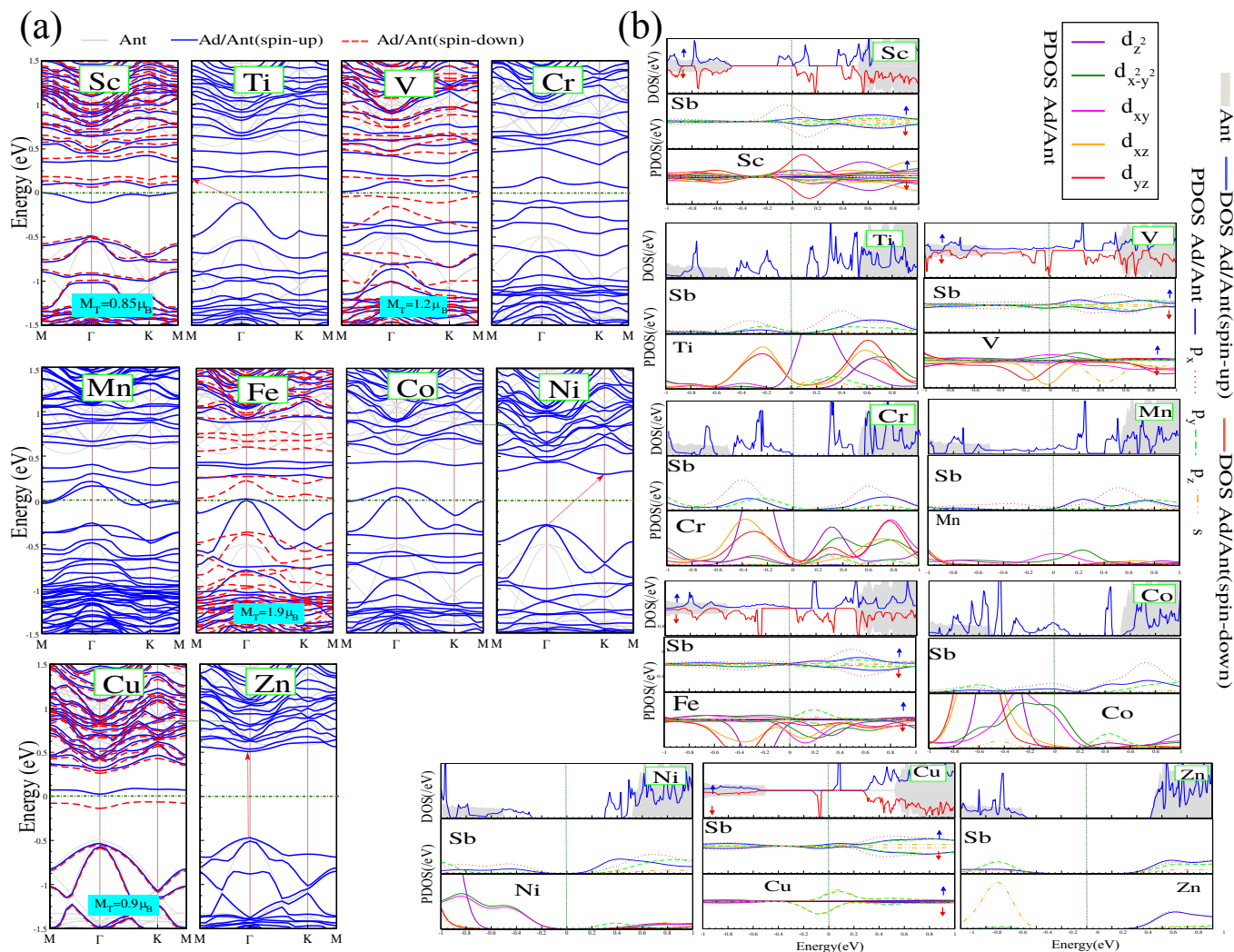
Fig. 6 (a) Electronic structure with corresponding (b) DOS and PDOS for adsorption of Sc, Ti, V, Cr, Mn, Fe, Co, Ni and Zn adatoms on antimonene at stable sites. The zero of energy is set to the E_F.

at E_F belongs to the Sb-$p_{x,y,z}$-orbitals around the missing atom, which confirms the metallic behavior of SV-ant and the fact that the magnetism is derived from these orbitals. For DV1-ant and DV2-ant, states appear around E_F and it exhibits a semiconductor with 0.76 and 0.72 eV band gaps, respectively. The VBM belongs to the Sb-$p_{x,y}$ orbital and the CBM belongs to the Sb-p_z orbital around the defect, which confirms the semiconducting behavior of these structures (see Figs. 8(f,g)). Finally, the SW-ant becomes a semiconductor with a 0.67 eV band gap located at the Γ point. Moreover, the band becomes flatter, indicating a strongly localized charge around these defects. We can see that the VBM of SW-ant originates from Sb-$p_{x,y}$-orbital and CBM belongs to the Sb-$p_{x,y,z}$-orbital around the defect. We simulated STM images of the adsorption of H, P, B, and Ti adatoms and different defects on antimonene (see Figs. S3(a-h)). We can see that the Sb atoms appear as white spots, however, the regions around H, P, B, and Ti adatoms and different defects correspond to the brighter spot.

6 Substitution of atom

In order to investigate atom substitution, we considered that O, S, F, Cl, N ,P, As, Bi, Li, Na, K, Be, Mg, and Ca atoms are replaced with the Sb host atom of antimonene. Hereafter, the atom substitued antimonene will be labeled as sub-ant. In Fig. S(4), a side view of the optimized structures with corresponding bond lengths between the substituted atom and its nearest Sb atom are shown. Difference charge density is indicated in the same panel. As shown in the figure, the bond lengths between the Sb and substituted Be, O, N, P, and S atoms, are shorter than the original Sb-Sb bond length because of the smaller radius and stronger electronegativity. The Bi, Na, and K atoms have a larger radius and weaker electronegativity and the bond lengths formed around Sb atoms are relatively larger. Therefore, after the substitution of these atoms, the antimonene structures show local deformation. These results are consistent with those presented in previous reports.[54,83] We calculated the electronic structure of atoms-substituted antimonene, as shown in Fig. 9, while the insets show top views of the optimized structures. Our calculations
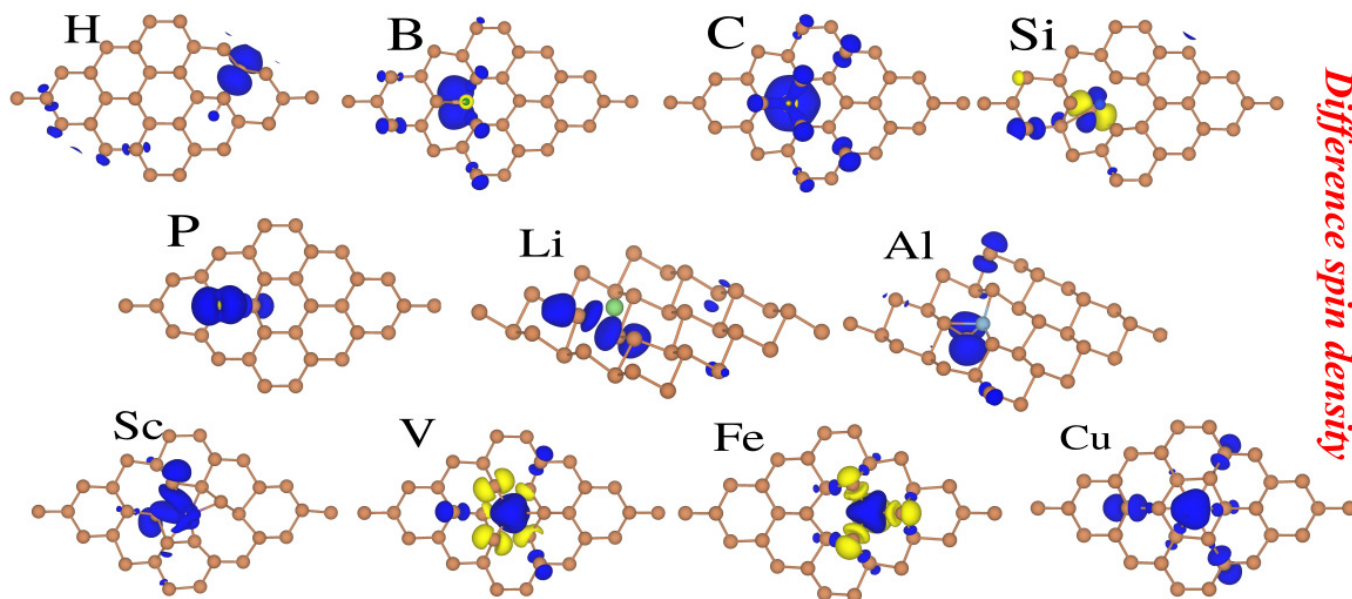
Fig. 7 Difference charge densities for the adsorption of H, B, C, Si, P, Li, Al, Sc, V, Fe and Cu adatoms on antimonene at stable sites. The blue and yellow regions represent the ↑ and ↓ spin states, respectively.
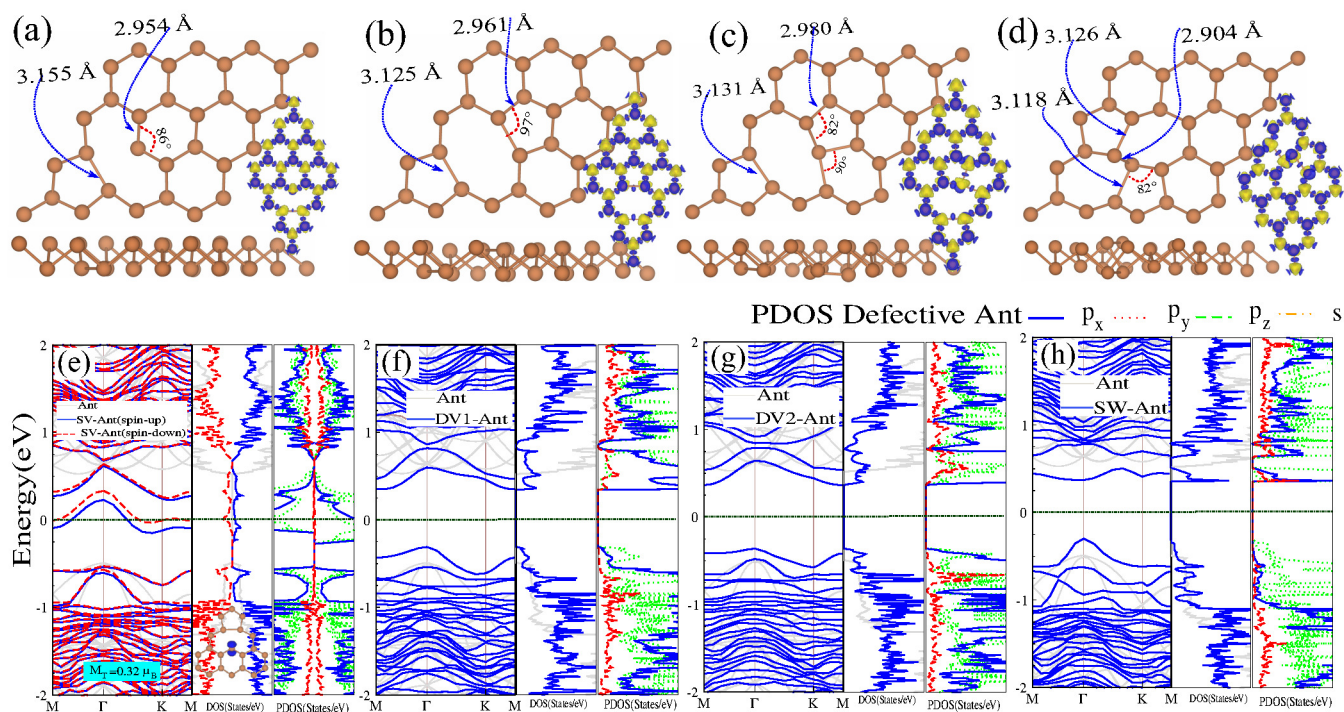

Fig. 8 Optimized structures with corresponding bond lengths and bond angles for (a) single vacancy, (b,c) double vacancy, and (d) Stone–Wales defects on antimonene. Electronic structure, DOS and PDOS of (e) single vacancy, (f,g) double vacancy and (l) Stone–Wales defects on antimonene. The zero of energy is set to E_F.

show that the O and S-ant exhibits a metallic character. Meanwhile, tt is easy to see that F and Cl-ant become semiconductors with indirect band gaps of 0.80 eV and 0.60 eV, respectively. The VBM and CBM of F and Cl-ant are located at the **M** point and between the **M**-Γ and **M**-**K** points directions, respectively. After

the doping of group-VA atoms in the antimonene, all of the new structures show the semiconducting property. The N-ant has a 0.75 eV direct band gap, while P, As, and Bi-ant exhibit an indirect semiconductor with a ~ 1 eV band gap. In pristine antimonene, each Sb atom forms covalent σ–Ń bonds wit the three nearest
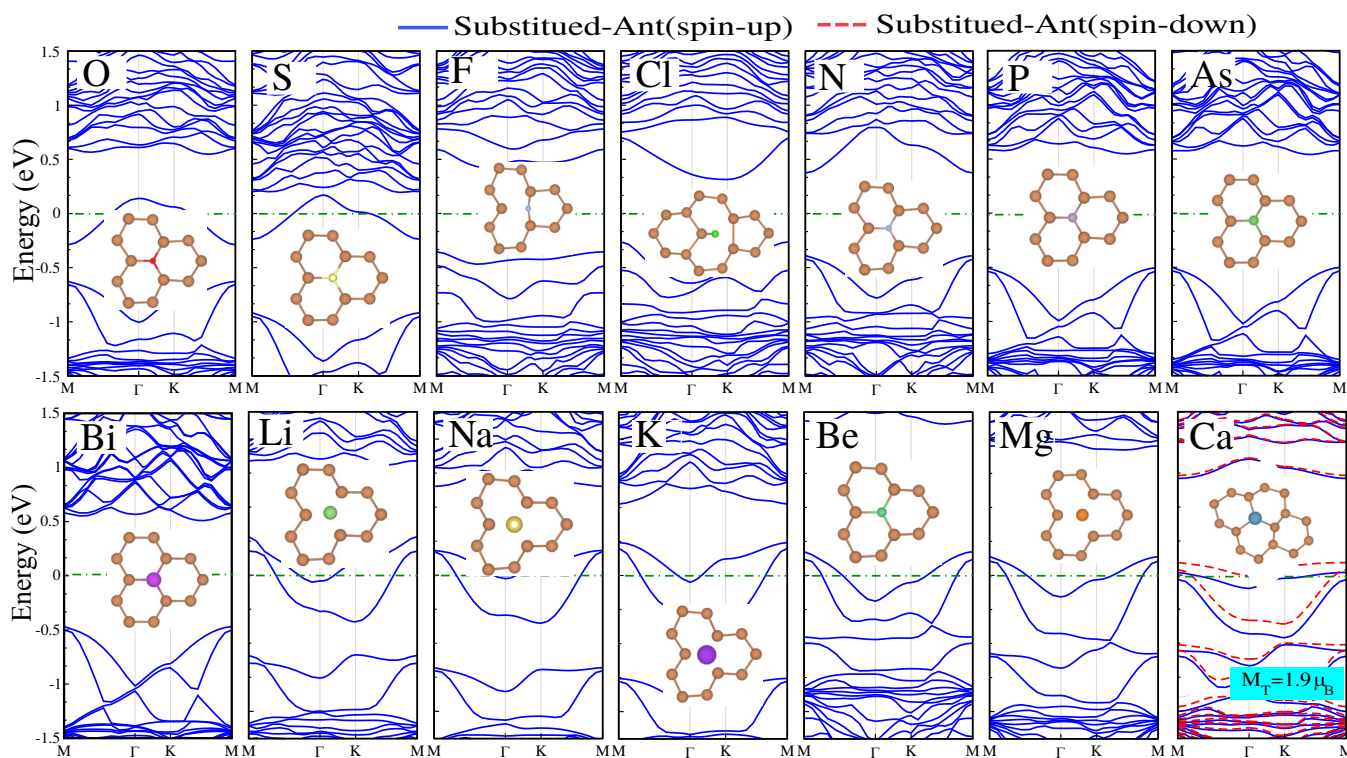
Fig. 9 Electronic structure of O, S, F, Cl, N , P, As, Bi, Li, Na, K, Be, Mg and Ca atoms substituted with Sb atom of antimonene. The insets are top view of optimized structures. The zero of energy is set to the E_F.

Sb atoms and leaves one lone pair of electrons, meaning that the bonds of pristine antimonene are saturated. In the case of N-ant, each N atom contributes three valence electrons to bond with the three nearest Sb atoms. The valence electrons of N are equal to the Sb atom, which retains the saturated bonds of sub-ant and exhibits a semiconducting character. However, in the O and S-ant, the saturated bonds of antimonene are missing. One non-bonding electron is left, and the E_F crosses the defect band. The system displays the metallic character. Thus, the VBMs of O and S-ant are unfilled and the defect band is localized at the E_F, since these antimonene form unsaturated metallic bonds. Notably, the VBM is evidently unfilled which indicates a metallic character for Li, Na, K, Be, Mg, and Ca-ant.

We found that, with the substitution of Ti, V, Mn, Fe and Co atoms, the atomic structure of antimonene can be kept very well, while other substitution, such as with Sc and Cr atoms, gives rise to a noticeable local deformation in the antimonene. The optimized structures for the TMs-antimonene, are shown in Fig. 10(a). For Sc, Ti, V, Cr, Mn, Fe, Co, Ni, and Zn-ant, the bond lengths vary between 2.55 to 2.91 Å. Our calculation results are consistent with those presented by previous reports.[83–85] It should be noted that the Sb-Sb bond length is 2.95 Å, after the Ti, V, Mn, Fe, and Co-ant, which is similar to the pristine antimonene bond length. In addition, the lattice constants of TMs-ant are also very close to the value of 16.84 Å found in antimonene. Consequently, we can conclude that, following the substitution of the TM atoms, the geometry of antimonene can be well kept. The electronic structure of the TMs-ant is shown in Fig. 10(b).

The substitution of TM atoms leads to some localized states in

the fundamental band gap due to the variation in electron distortion in the antimonene. The Sc, Cr, and Co-ant become semiconductors, and Sc-ant has the indirect band gap of 0.86 eV while Cr and Co-ant have direct band gaps of 0.65 eV and 0.57 eV, respectively. For Ti-ant, the spin polarization is observed and induces a 1 μ_B magnetic moment. Both the ↑ and ↓ spin channels were found to be semiconducting. Thus, the spin-polarized semiconducting state can be realized in the Ti-ant system. The V-ant, becomes a half-metal with a 2 μ_B magnetic moment, and for this structure, the band gap in the semiconducting spin channel is 0.98 eV, which indicates the robust stability of the half-metallic property. The Mn and Fe-ant exhibit a ferromagnetic-metal and induce magnetic moments of 2 and 2.6 μ_B, respectively to the antimonene, while Ni-ant is a metal. For Cu and Zn-ant, the situation was quite different, as they represent a metallic character and there is not any magnetism in their ground states. As a result, the electronic property of antimonene can be easily tuned. Depending on the kinds of impure atoms, TMs-ant can be a half-metal, spin-polarized semiconductor or metal. In order to further elucidate the magnetic states of the doped systems, the difference spin densities are plotted in Fig. 11(d). The blue and yellow regions represent the ↑ and ↓ spin states, respectively. Clearly, in Ti, V, Mn, Fe and Ni-ant the spin density is entirely localized at TM impurity. The order of magnetic coupling in V, Mn, Fe-ant is antiferromagnetic material. These magnetic properies may be useful for the applications of spintronics and magnetic storage.
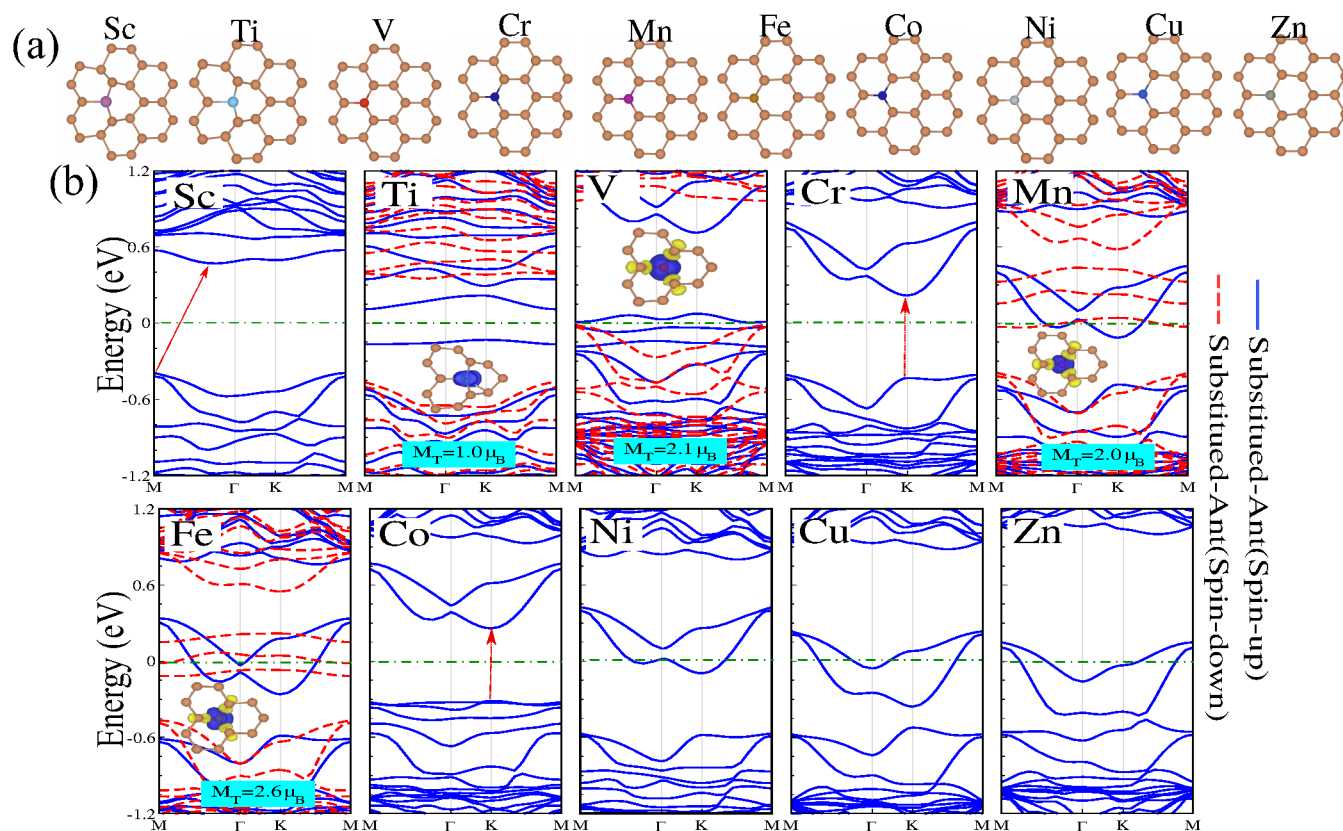
Fig. 10 (a) Top view of optimized structures and (b) electronic structures for Sc, Ti, V, Cr, Mn, Fe, Co, Ni and Zn atoms substituted antimonene. The zero of energy is set to E_F. The difference spin densities are shown in the insets. The blue and yellow regions represent the ↑ and ↓ spin states, respectively.

7 Strain engineering

Strain engineering is a robust method for tuning electronic properties and topological natures in 2DM, and thus it is interesting to investigate these effects in antimonene nanosheet. Thus, we investigate the effects of uniaxial/biaxial strains (in tensile and compression states) on antimonene. While maintaining the crystal symmetry, the tensile and compression strains are defined as $\varepsilon = (a - a_0)/a_0 \times 100$, where a ($a_0$) is strained (non-strained) lattice constants. Uniaxial strain is applied along zigzaging directions, while biaxial strain is applied along the a-b axis. The variations of bond length and lattice constant as functions of strain are shown in Fig. 11(a). The band structures under the uniaxial and biaxial strains are respectively shown in Figs. 11(b,c). We can see that the energy band gap can be modified significantly by strain, implying that the interatomic coupling can tune the topological natures of antimonene These results are consistent with those presented by previous studies.[59,63] For antimonene, under 0 % ≤ uniaxial ≤ +4%, the band gap increases monotonically, this situation is different from the SOC effect and we can see that band gap decreases. For large uniaxial strain (> +4%) with/without the SOC effect, an indirect-direct band gap transition occurs, Without SOC effect, we see that under 0 % ≤ biaxial ≤ +8%, the band gap value increases and decreases. Meanwhile, an indirect-direct band gap transition occurs at a moderate strain level of ≥10%. Under uniaxial/biaxial strains from 0 to -8%, the

CBM is continuously shift downward to the E_F, while the VBM increases reversibly, leading the band gap to decrease monotonically in the cases both with and without SOC effect. For biaxial strain with -4 and -6%, the CBM shifted from **M** to **K** points. However for the biaxial strain, where the critical value reaches up to $> -8\%$, we can see a semi-metallic state with zero density of states at the E_F and for large uniaxial/biaxial strains ($> -8\%$), a metal-semiconductor transition occurs. The effect of SOC on the electronic structure is found to be significant such the that degeneracies at the VBM are removed. The variations of the band gap as functions of uniaxial and biaxial strains with and without spin orbital coupling, are shown in Figs. 11(d,e).

8 Electric field

From the perspective of potential device applications, the ability to control topological electronic properties by controlling the Fermi-level via electric field, charging is highly desirable. The existence of buckling in the antimonene, leads to to a potential difference between the two atomic sublattices, which turns out to potentially intrinsically useful in modulating the electronic structure in terms of a perpendicular electric field.[59,65] We present the effect of the electric field on the H/ant. The electronic structure of H/ant as a function of electric field is shown in Fig. 12(a), In **F** = +0.1 and -0.1 V/Å, the charge on the H decreases and increases with changing **F** value, and the excess electronic charge

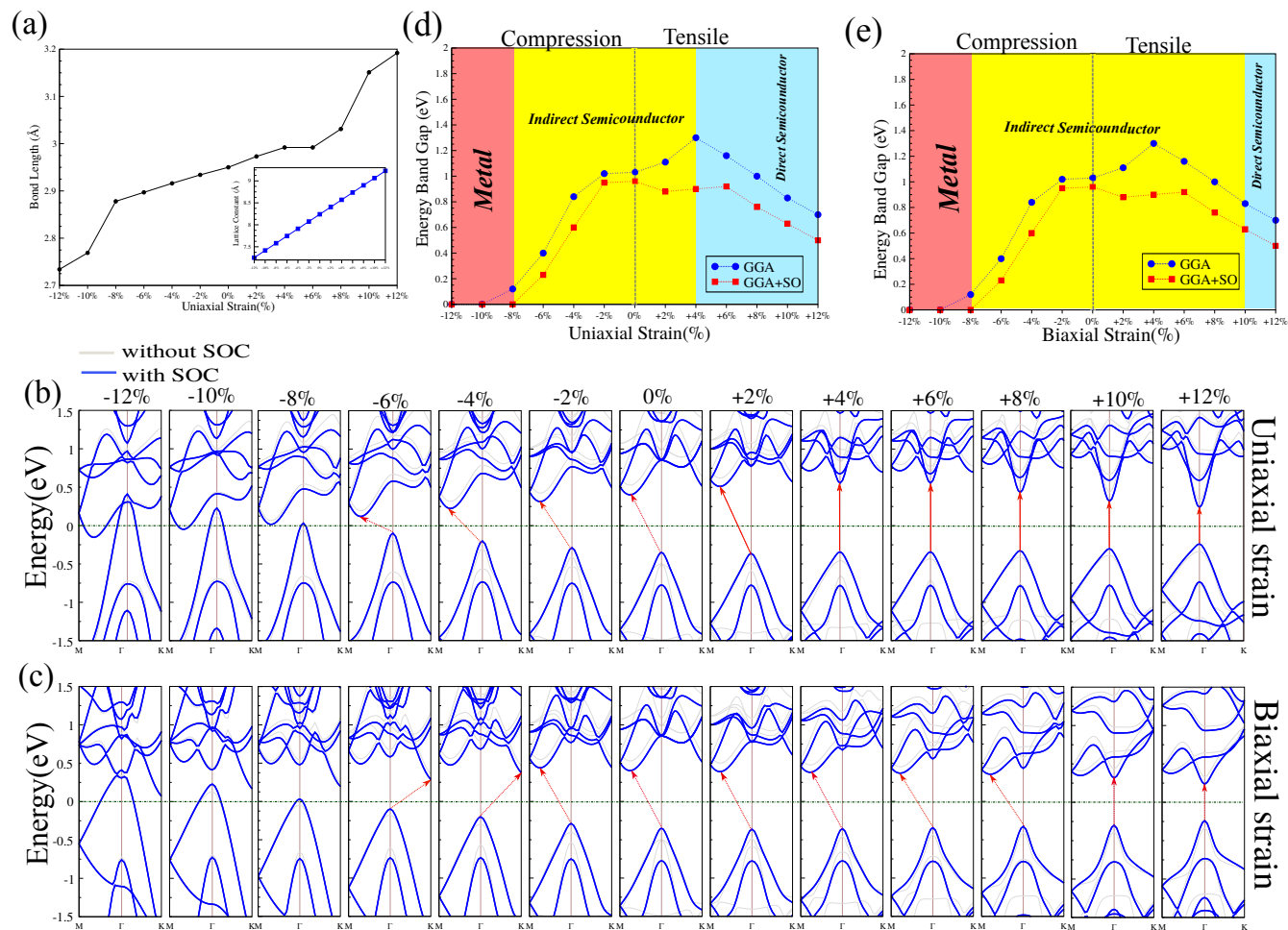Physical Chemistry Chemical Physics Accepted Manuscript

Fig. 11 (a) Variations of bond length and lattice constant as functions of strain. (b,c) Electronic structure of antimonene with uniaxial and biaxial strains with and without spin orbital coupling. (d,e) Energy band gap of antimonene as a function of (d) uniaxial and (e)biaxial strains. The zero of energy is set to E_F

on the H is transferred from nearby Sb atoms of antimonene and enhances the electronic potential at the H atom. Our results show that the magnetic moment of H/ant decreases to 0.75 μ_B (+0.1 V/Å), and increases to 0.85 μ_B (-0.1 V/Å). In both cases, it retain its half-metallic property. The band structure of antimonene as a function of charging is shown in Fig. 12(b). As shown, we can affect the Fermi level of the antimonene by charging the material. For q = +0.2 e, the Fermi level shifts in to the VB and creates holes, while for q = -0.2 e, the Fermi level shifts in to the CB and creates electrons.

9 Conclusion

In summary, based on the first-principles calculations, we investigate the structural, electronic and magnetic properties of adsorbed and substituted antimonene with various atoms such as H, O, S, ,F ,Cl, B, C, Si, N, P, Al, Li, Na, K, Be, Mg, Ca, Sc, Ti, V, Cr, Mn, Fe, Co, Ni, Cu, and Zn. Using these approaches, the electronic structure of antimonene can be modified. Adsorption and substitution may offer a variety of electronic behaviors including semiconductor (O, S, Be, Mg, Ca, Ti, Cr, Ni, and Zn), metal (F, Cl, N, Na, and K), half-metal (H and Fe), ferromagnetic-

metal (Si, Li, and Mn), dilute magnetic semiconductor (B, C, P, Sc, V, and Cu) and spin-glass semiconductor (Al). Upon the topological defects including vacancies and stone-wales, the electronic property of antimonene is modified. For single vacancy, localized, filled spin up states and empty spin-down states occur in the fundamental band gap, and a 0.3 μ_B magnetic moment is attained. Furthermore, we study the effects of electric field, strain, and charging. We found that, applied uniaxial and biaxial strains appears to lead to the direct semiconducting-indirect semiconducting-metallic transition of electronics structure with-/without spin-orbital coupling calculations. Our calculations suggest that the adsorption and substitution of atoms on antimonene, provides viable electronic and magnetic properties which can be useful in a variety of future applications such as, nanosensors, nanoelectronics and nanomagnetics devices. Moreover, with the existence of a tunable band gap and magnetism by electric field, charging and strain in antimonene is highly desirable for its use in nanoscale optoelectronic device applications.
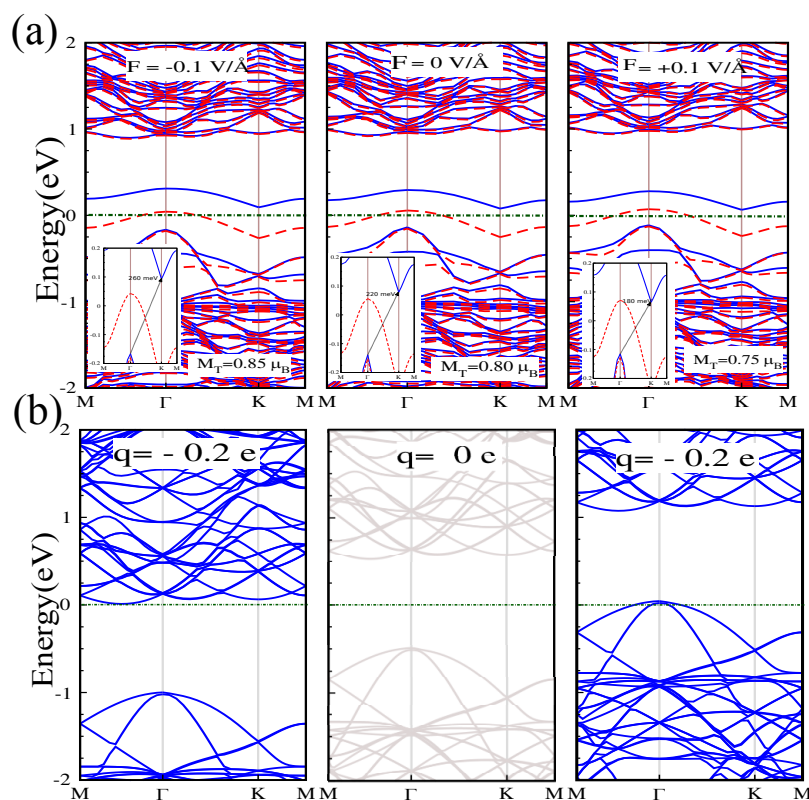
Fig. 12 Electronic structure of (a) H adsorbed on antimonene as a function of electric field and (b) antimonene as a function of charging. The **F**>0 and **F**<0 V/Å denote the electric fields parallel and antiparallel to the z-axis, respectively. q>0 e and q<0 e correspond to the chargings where one electron is removed from and added to the antimonene, respectively. The zero of energy is set to E_F

10 ACKNOWLEDGMENTS

References

1 K. S. Novoselov, A. K. Geim, S. V. Morozov, D. Jiang, Y. Zhang, S. V. Dubonos, I. V. Grigorieva and A. A. Firsov, *Science*, 2004, **306**, 666–669.

2 R. Roldan, L. Chirolli, E. Prada, J. A. Silva-Guillen, P. San-Jose and F. Guinea, *Chem. Soc. Rev.*, 2017, **46**, 4387–4399.

3 C. Lee, X. Wei, J. W. Kysar and J. Hone, *Science*, 2008, **321**, 385–388.

4 A. K. Geim and K. S. Novoselov, *Nature materials*, 2007, **63**, 183–91.

5 I. V. Geim, A. K.; Grigorieva, *Nature*, 2013, **499**, 419–425.

6 I. Lee, S. Rathi, D. Lim, L. Li, J. Park, Y. Lee, K. S. Yi, K. P. Dhakal, J. Kim, C. Lee, G.-H. Lee, Y. D. Kim, J. Hone, S. J. Yun, D.-H. Youn and G.-H. Kim, *Advanced Materials*, **28**, 9519–9525.

7 D. Wu, Y. Wang, F. Wang, H. Wang, Y. An, Z. Gao, F. Xu and K. Jiang, *Carbon*, 2017, **123**, 756 – 766.

8 A. A. Balandin, S. Ghosh, W. Bao, I. Calizo, D. Teweldebrhan, F. Miao and C. N. Lau, *Nano Letters*, 2008, **8**, 902–907.

9 Schedin F., Geim A. K., Morozov S. V., Hill E. W., Blake P., Katsnelson M. I. and Novoselov K. S., *Nature Materials*, 2007, **6**, 652.

10 Zhu Feng-feng, Chen Wei-jiong, Xu Yong, Gao Chun-lei, Guan Dan-dan, Liu Can-hua, Qian Dong, Zhang Shou-Cheng and Jia Jin-feng, *Nature Materials*, 2015, **14**, 1020.

11 S. Balendhran, S. Walia, H. Nili, S. Sriram and M. Bhaskaran, *Small*, 2015, **11**, 640–652.

12 A. Resta, T. Leoni, C. Barth, A. Ranguis, C. Becker, T. Bruhn, P. Vogt and G. Le Lay, *Scientific Reports*, 2013, **3**, 2399 EP –.

13 J. Gao, G. Zhang and Y.-W. Zhang, *Scientific Reports*, 2016, **6**, 29107 EP –.

14 Y. Xu, B. Yan, H.-J. Zhang, J. Wang, G. Xu, P. Tang, W. Duan and S.-C. Zhang, *Phys. Rev. Lett.*, 2013, **111**, 136804.

15 X. Han, H. M. Stewart, S. A. Shevlin, C. R. A. Catlow and Z. X. Guo, *Nano Letters*, 2014, **14**, 4607–4614.

16 Y. Ding, Y.; Wang, *Phys. Chem. Chem. Phys.*, 2015, **119**, 10610–10622.

17 K. T. Chan, J. B. Neaton and M. L. Cohen, *Phys. Rev. B*, 2008, **77**, 235430.

18 H. Sahin and F. M. Peeters, *Phys. Rev. B*, 2013, **87**, 085423.

19 Q. Pang, L. Li, L. li Zhang, C. ling Zhang and Y. ling Song, *Canadian Journal of Physics*, 2015, **93**, 1310–1318.

20 Y. Li, C. Xia, J. Du, W. Xiong, X. Li and S. Wei, *Phys. Chem. Chem. Phys.*, 2017, **19**, 5423–5429.

21 M. Lalitha, S. S. Mahadevan and S. Lakshmipathi, *Journal of Materials Science*, 2017, **52**, 815–831.

22 T. L. W. A. R. Naqvi, S. R.; Hussain, *Phys. Chem. Chem. Phys.*, 2017, **121**, 7667âĂŞ7676.

23 F. Ersan, H. Arkin and E. Aktrk, *RSC Adv.*, 2017, **7**, 37815–37822.

24 F. Li, H. Wu, Z. Meng, R. Lu and Y. Pu, *The Journal of Physical Chemistry Letters*, 2019, **10**, 761–767.

25 M. Sun, Q. Ren, Y. Zhao, S. Wang, J. Yu and W. Tang, *Journal of Applied Physics*, 2016, **119**, 143904.

26 Y. Kadioglu, F. Ersan, G. GÃűkoÄ§lu, O. ÃIJzengi Akturk and E. Akturk, *Materials Chemistry and Physics*, 2016, **180**, 326 – 331.

27 F. Ersan, Ã. Arslanalp, G. GÃűkoÄ§lu and E. Akturk, *Applied Surface Science*, 2014, **311**, 9 – 13.

28 F. Ersan, A. G. GÃűkÃğe and E. Akturk, *Applied Surface Science*, 2016, **389**, 1 – 6.

29 S. Zhang, M. Xie, B. Cai, H. Zhang, Y. Ma, Z. Chen, Z. Zhu, Z. Hu and H. Zeng, *Phys. Rev. B*, 2016, **93**, 245303.

30 S. Zhang, W. Zhou, Y. Ma, J. Ji, B. Cai, S. A. Yang, Z. Zhu, Z. Chen and H. Zeng, *Nano Letters*, 2017, **17**, 3434–3440.

31 Ji Jianping, Song Xiufeng, Liu Jizi, Yan Zhong, Huo Chengxue, Zhang Shengli, Su Meng, Liao Lei, Wang Wenhui, Ni Zhenhua, Hao Yufeng and Zeng Haibo, *Nature Communications*, 2016, **7**, 13352.

32 P. Ares, F. Zamora and J. Gomez-Herrero, *ACS Photonics*, 2017, **4**, 600–605.

33 K.-X. Chen, S.-S. Lyu, X.-M. Wang, Y.-X. Fu, Y. Heng and D.-C. Mo, *The Journal of Physical Chemistry C*, 2017, **121**, 13035–13042.

34 Y. Hu, Y. Wu and S. Zhang, *Physica B: Condensed Matter*, 2016, **503**, 126 – 129.

35 Y. Wang, P. Huang, M. Ye, R. Quhe, Y. Pan, H. Zhang, H. Zhong, J. Shi and J. Lu, *Chemistry of Materials*, 2017, **29**, 2191–2201.

36 V. Nagarajan and R. Chandiramouli, *Physica E: Low-dimensional Systems and Nanostructures*, 2018, **97**, 98 – 104.

37 H. V. Phuc, N. N. Hieu, B. D. Hoi, L. T. Phuong, N. V. Hieu and C. V. Nguyen, *Superlattices and Microstructures*, 2017, **112**, 554 – 560.

38 Y. Kadioglu, J. A. Santana, H. D. ÃŰzaydin, F. Ersan, O. Ã. Aktürk, E. Aktürk and F. A. Reboredo, *The Journal of Chemical Physics*, 2018, **148**, 214706.

39 O. U. Aktürk, V. O. Özçelik and S. Ciraci, *Phys. Rev. B*, 2015, **91**, 235446.

40 A.-X. Zhang, J.-T. Liu, S.-D. Guo and H.-C. Li, *Phys. Chem. Chem. Phys.*, 2017, **19**, 14520–14526.

41 Y. Wang and Y. Ding, *Phys. Chem. Chem. Phys.*, 2015, **17**, 27769–27776.

42 S. Pakdel, M. Pourfath and J. J. Palacios, *Beilstein J. Nanotechnol.*, 2018, **9**, 1015âĂŞ1023.

43 Q. Pang, L. Li, C.-L. Zhang, X.-M. Wei and Y.-L. Song, *Materials Chemistry and Physics*, 2015, **160**, 96 – 104.

44 M.-Y. Liu, Q.-Y. Chen, Y. Huang, Z.-Y. Li, C. Cao and Y. He, *Nanotechnology*, 2018, **29**, 095203.

45 G. Zhang, X. Tang, X. Fu, W. Chen, B. Shabbir, H. Zhang, Q. Liu and M. Gong, *Nanoscale*, 2019, **11**, 1762–1769.

46 J. Wang, T. Yang, Z. Zhang and L. Yang, *Applied Physics Letters*, 2018, **112**, 213104.

47 K. H. Yeoh, T. L. Yoon, D. S. Ong, T. L. Lim and Y. Zuntu Abdullahi, *Phys. Chem. Chem. Phys.*, 2017, **19**, 25786–25795.

48 F. Ersan, E. Aktürk and S. Ciraci, *The Journal of Physical Chemistry C*, 2016, **120**, 14345–14355.

49 O. "Uzengi AktÃijrk, E. AktÃijrk and S. Ciraci, *Phys. Rev. B*, 2016, **93**, 035450.

50 R. Meng, M. Cai, J. Jiang, Q. Liang, X. Sun, Q. Yang, C. Tan and X. Chen, *IEEE Electron Device Letters*, 2017, **38**, 134–137.

51 A. Sengupta and T. Frauenheim, *Materials Today Energy*, 2017, **5**, 347 – 354.

52 L. Yang, Y. Song, W. Mi and X. Wang, *RSC Adv.*, 2016, **6**, 66140–66146.

53 L. Yang, W. Mi and X. Wang, *RSC Adv.*, 2016, **6**, 38746–38752.

54 Y. Hu, T. Shu, C. Mao, L. Xue, Z. Yan and Y. Wu, *Physica B: Condensed Matter*, 2019, **553**, 195 – 201.

55 M. Xie, S. Zhang, B. Cai, Y. Zou and H. Zeng, *RSC Adv.*, 2016, **6**, 14620–14625.

56 X. Liang, S.-P. Ng, N. Ding and C.-M. L. Wu, *Applied Surface Science*, 2018, **443**, 74 – 82.

57 X. Sun, Y. Liu, Z. Song, Y. Li, W. Wang, H. Lin, L. Wang and Y. Li, *J. Mater. Chem. C*, 2017, **5**, 4159–4166.

58 X. Liu, L. Liu, L. Yang, X. Wu and P. K. Chu, *The Journal of Physical Chemistry C*, 2016, **120**, 24917–24924.

59 Zhao Mingwen, Zhang Xiaoming and Li Linyang, *Scientific Reports*, 2015, **5**, 16108.

60 H. V. Phuc, N. N. Hieu, B. D. Hoi, L. T. Phuong, N. V. Hieu and C. V. Nguyen, *Superlattices and Microstructures*, 2017, **112**, 554 – 560.

61 S. Zhang, Z. Yan, Y. Li, Z. Chen and H. Zeng, *Angewandte Chemie International Edition*, **54**, 3112–3115.

62 C. Wang, Q. Xia, Y. Nie, M. Rahman and G. Guo, *AIP Advances*, 2016, **6**, 035204.

63 D. R. Kripalani, A. A. Kistanov, Y. Cai, M. Xue and K. Zhou, *Phys. Rev. B*, 2018, **98**, 085410.

64 M. Abid, A. Shoaib, M. H. Farooq, H. Wu, D. Ma and B. Fu, *Journal of Physics and Chemistry of Solids*, 2017, **110**, 167 – 172.

65 Song Yan, Wang Xiaocha and Mi Wenbo, *npj Quantum Materials*, 2017, **2**, 15.

66 F. Zhang, W. Li and X. Dai, *Superlattices and Microstructures*, 2016, **100**, 826 – 832.

67 W. Zhang, W. He, J. Zhao and C. He, *Journal of Solid State Chemistry*, 2018, **265**, 257 – 265.

68 M. M. Dong, C. He and W. X. Zhang, *J. Mater. Chem. C*, 2017, **5**, 3830–3837.

69 H. Zeng, J. Zhao, A.-Q. Cheng, L. Zhang, Z. He and R.-S. Chen, *Nanotechnology*, 2018, **29**, 075201.

70 J. P. Perdew, K. Burke and M. Ernzerhof, *Phys. Rev. Lett.*, 1996, **77**, 3865–3868.

71 T. Ozaki, *Phys. Rev. B*, 2003, **67**, 155108.

72 T. Ozaki and H. Kino, *Phys. Rev. B*, 2004, **69**, 195113.

73 N. Troullier and J. L. Martins, *Phys. Rev. B*, 1991, **43**, 1993–

2006.

74 R. S. Mulliken, *The Journal of Chemical Physics*, 1955, **23**, 2343–2346.

75 P. Giannozzi, S. Baroni, N. Bonini, M. Calandra, R. Car, C. Cavazzoni, D. Ceresoli, G. L. Chiarotti, M. Cococcioni, I. Dabo, A. D. Corso, S. de Gironcoli, S. Fabris, G. Fratesi, R. Gebauer, U. Gerstmann, C. Gougoussis, A. Kokalj, M. Lazzeri, L. Martin-Samos, N. Marzari, F. Mauri, R. Mazzarello, S. Paolini, A. Pasquarello, L. Paulatto, C. Sbraccia, S. Scandolo, G. Sclauzero, A. P. Seitsonen, A. Smogunov, P. Umari and R. M. Wentzcovitch, *Journal of Physics: Condensed Matter*, 2009, **21**, 395502.

76 J. M. Soler, E. Artacho, J. D. Gale, A. GarcÃ■a, J. Junquera, P. OrdejÃşn and D. SÃ₄nchez-Portal, *Journal of Physics: Condensed Matter*, 2002, **14**, 2745.

77 X. Gonze, B. Amadon, P.-M. Anglade, J.-M. Beuken, F. Bottin, P. Boulanger, F. Bruneval, D. Caliste, R. Caracas, M. CÃŕtÃľ, T. Deutsch, L. Genovese, P. Ghosez, M. Giantomassi, S. Goedecker, D. Hamann, P. Hermet, F. Jollet, G. Jomard, S. Leroux, M. Mancini, S. Mazevet, M. Oliveira, G. Onida, Y. Pouillon, T. Rangel, G.-M. Rignanese, D. Sangalli, R. Shaltaf, M. Torrent, M. Verstraete, G. Zerah and J. Zwanziger, *Computer Physics Communications*, 2009, **180**, 2582 – 2615.

78 H. J. Monkhorst and J. D. Pack, *Phys. Rev. B*, 1976, **13**, 5188–5192.

79 J. Tersoff and D. R. Hamann, *Phys. Rev. Lett.*, 1983, **50**, 1998–2001.

80 I. Horcas, R. FernÃ₄ndez, J. M. GÃşmez-RodrÃ■guez, J. Colchero, J. GÃşmez-Herrero and A. M. Baro, *Review of Scientific Instruments*, 2007, **78**, 013705.

81 Pizzi Giovanni, Gibertini Marco, Dib Elias, Marzari Nicola, Iannaccone Giuseppe and Fiori Gianluca, *Nature Communications*, 2016, **7**, 12585.

82 E. T. H. A. Jahn, *Proceedings of the Royal Society of London A: Mathematical, Physical and Engineering Sciences*, 1937, **161**, 220–235.

83 Y. Hu, T. Shu, C. Mao, L. Xue, Z. Yan and Y. Wu, *Physica B: Condensed Matter*, 2018.

84 Y. Zhou and X. Lin, *Applied Surface Science*, 2018, **458**, 572 – 579.

85 C. He, M. Cheng and W. Zhang, *Materials Research Express*, 2018, **5**, 065059.

Physical Chemistry Chemical Physics Accepted Manuscript